Elucidation of Real-Time Hardening Mechanisms of Two Novel High-Strength Calcium Phosphate Bone Cements

Valery V. Smirnov,[1] Julietta V. Rau,[2] Amanda Generosi,[2] Valerio Rossi Albertini,[2] Daniela Ferro,[3] Sergey M. Barinov[1]

[1] Baikov Institute of Metallurgy and Materials Science, Russian Academy of Sciences, Moscow 119991, Russia

[2] Istituto di Struttura della Materia, CNR, Via del Fosso del Cavaliere, 100-00133 Rome, Italy

[3] Istituto per lo Studio dei Materiali Nanostrutturati, CNR, Piazzale Aldo Moro, 5-00185 Rome, Italy

Abstract: Despite the numerous literature data available in the field of calcium phosphate bone cements, the mechanism and kinetics of their hardening, both of which are of great importance for cements application, in most cases, is unknown. In this work, the mechanism and kinetics of hardening of two novel high-strength calcium phosphate bone cements were studied using the energy dispersive X-ray diffraction technique, which allows rapid collection of the patterns. The phase transformations occurring on the setting and hardening processes were monitored *in situ*. Containing minimal quantity of components, whose mixing leads to the formation of cements with pH close to neutral, the cements under study are simple in handling. The main component of both formulations is tetracalcium phosphate. In both cements, the effect of the addition of high- and low-molecular weight chitosan on phase development and kinetics was investigated in detail. One of the cements has the compressive strength of about 70 MPa, whereas the strength of the other, containing $Ca_3Al_2O_6$, is much higher, about 100 MPa. This latter cement could be regarded as an alternative to the common low-strength bioresorbable brushite cements. © 2009 Wiley Periodicals, Inc. J Biomed Mater Res Part B: Appl Biomater 93B: 74–83, 2010

Keywords: bone cement; calcium phosphate cement; chitosan; X-ray diffraction; crystallization

INTRODUCTION

In recent years, considerable efforts have been focused on the development of calcium phosphate cements (CPC) used as injectable bone substitutes because of their favorable tissue responses. Since their discovery in 1980s,[1,2] many commercial compositions were introduced in clinical practice and are currently in use.[3–5] Despite the long history of CPCs and numerous publications in the field, there is still a lack of studies of their basic properties such as mechanism of setting and hardening reactions and their kinetics, both of which are of great importance for cements application. The traditional approach to characterize the setting reaction of a cement is mechanical: a cement is considered to be set when it can resist to a given mechanical load applied onto its surface (a Vicat test). However, cements can sometimes exhibit two or more hardening reactions, so that additional techniques to follow the setting and hardening processes more accurately may be useful.[6]

In our previous works,[7,8] the energy dispersive X-ray diffraction (EDXRD) technique has proved to be a suitable tool to investigate the kinetics during the cements setting and hardening. In this work, this method is applied to study the phase transformations and kinetics of hardening of two novel CPCs intended for possible use in orthopedic applications. The diffraction patterns from the cement pastes were collected *in situ*, starting from 1 min from the beginning of the process. Tetracalcium phosphate (TetCP) is the main component of both cements,[2] and one of them also contains calcium aluminate to enhance its compressive strength. The compressive strength and the pH value changes for both cements were registered during the hardening period. In both cements, the effect of the addition of low- and high-molecular weight chitosan on the phase development kinetics was studied. Low-molecular weight chitosan is known to inhibit the hardening process in the TetCP and other calcium phosphate-based cements.[8,9]

MATERIALS AND METHODS

Two different cement powders were prepared, both based on TetCP, $Ca_4(PO_4)_2O$, powder. To obtain cement powder 1, calcium oxide and ammonium hydrophosphate powders were mixed in a planetary ball mill for 30 min, using corundum balls. After that, the powders mix was heat treated at $1500°C$ for 2 h in an air furnace to initiate the following reaction of TetCP formation:

$$4CaO + 2(NH_4)_2HPO_4 \rightarrow Ca_4(PO_4)_2O + 4NH_3 + 3H_2O \quad (1)$$
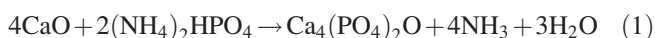
Analytical grade starting reagents were used. CaO reagent was used in approximately 10% mass excess, so that it was not completely consumed in the reaction (1), and its presence was detected in the precursor powders. The reaction product was grinded in a ball mill to the mean particle size of about 10 ± 2 μm, measured by an optical microscopy (microscope Neophot-32 Carl Zeiss). Conventional angular dispersive X-ray diffraction (Diffractometer Shimadzu XRD-6000, $CuK_{\alpha 1}$ radiation, JCPDS data base) and petrographic (optic microscope Biolam-M) analyses showed that the powders were composed of TetCP, containing a minor amount of CaO (about 5–7 wt %), as determined using a calibration curve.

To prepare cement powder 2, the same synthesis procedure was applied as for cement powder 1, and then, an admixture of finely powdered calcium aluminate, $Ca_3Al_2O_6$ (25 wt %), was introduced.

Hardening liquid was a saturated aqueous solution of magnesium phosphate ($MgHPO_4$) prepared by reaction of magnesium carbonate ($MgCO_3$) with phosphoric acid (H_3PO_4). The hardening liquid contained 6–8 wt % of Mg^{2+} ions and 40–43 wt % of PO_4^{3-} groups. Its pH was around 2.0–2.4.

To obtain the cement pastes 1 and 2, the powders 1 and 2 (0.4 g) were mixed intensively (approximately for 1 min) with the hardening liquid (0.2 mL) on a glass plate, until a dense homogeneous creamy paste was formed.

Both water-soluble, low-molecular weight (38.2 kDa) chitosan (75% deacetilation degree) and acid-soluble (pH < 6.5), high-molecular weight (478 kDa) chitosan (79% deacetilation degree) were supplied by "IREA 2000" chemical company (Russia).

The cements containing chitosan were prepared by adding 0.01 g of low- or high-molecular weight chitosan to the cement precursor powder 1 or 2. Subsequently, to this mixture, the hardening liquid was added, and an intensive mixing for approximately 1 min was performed. The same cement powder/hardening liquid ratio, as described above, was used.

The pastes were poured into a 8-mm diameter Teflon container. After setting, the cements samples were removed from the container, added to a physiological isotonic 0.9% NaCl solution, and placed in a thermostatic furnace at $37°C$. Setting time of pastes was evaluated by means of a

1-mm tip diameter Vicat needle meter with 400-g lead (according to ISO standard 1566). The cement is considered set when the needle fails to make a perceptible circular indentation on the cement surface. The setting time for cement 1 was 4–6 min, for cement 1 with the addition of low-molecular weight chitosan—15–20 min, whereas for cement 1 with the addition of high-molecular weight chitosan—20–25 min. Without chitosan, the setting time for cement 2 was longer (6–8 min), and with the addition of chitosan, the same as for the cement 1 with the addition of chitosan.

Cements 1 and 2 could be considered as relatively dense, their porosity being about 10–20% according to the density measurements.

The compressive strength was determined for 8×16 mm cement samples, the ratio being 1:2, according to the common standard procedure for the compressive strength testing.[10] Wet specimens (after 72 h aging in physiological solution) were loaded into an Instron 5581 testing machine at the cross-head speed of 0.1 mm/min.

The pH measurements were performed as follows: samples (1 g) of crushed cements (<100 μm particle size), after 0.5–22 days of sustaining in a physiological solution at $37°C$, were placed into a 50-mL volume flask, and distilled water was added to a 50-mL volume. pH value was measured after an intense mixing of the solution using a Hanna Instruments HI 8314 pH meter.

Scanning electron microscopy (SEM) (a LEO 1420 apparatus), coupled with a system for microanalysis (energy dispersive X-ray spectroscopy) INCA, was applied for the morphological studies of cement samples.

Subsequently, the EDXRD method was applied to follow in real-time the structural modifications taking place on cements hardening, by collecting sequences of diffraction patterns. The acquisition time of each pattern was set at 60 s, and the overall observation time was 72 h. The EDXRD measurements were performed by a noncommercial apparatus, based on the use of a nonmonochromatized ("white") primary X-ray beam produced by a W-anode (supplied at 55 kV) and an ultra pure Ge solid-state detector, which is not only able to count the number of diffracted photons but also measure the energy of each of them. In this way, the reciprocal space scan necessary to reconstruct the diffraction pattern, that is, the scan of the scattering parameter $q = a\,E\,\sin\theta$ (where q is the normalized momentum transfer magnitude, a is a constant, E is the energy of the incident X-ray beam, and 2θ is the scattering angle), is performed electronically.[11,12] The main advantage of the energy dispersive mode over its conventional angular dispersive counterpart in performing the X-ray diffraction experiments is that the geometric setup is kept fixed during the acquisition of the patterns, which simplifies the experimental geometry and prevents systematic angular errors as well as possible misalignments. In particular, this technique provides faster recording of the Bragg peaks because, in the ED mode, the whole diffraction pattern is obtained in parallel at any q value.

Several diffraction patterns were collected as preliminary tests on the pristine cement powders 1 and 2 and chitosan (38.2 and 478 kDA), at various scattering angles, to make a wide q-scan for individuating the q-region of interest and making an accurate attribution of the diffracted intensities. Because, according to the value of the high voltage supply reported above, the maximum beam energy corresponds to 55 kV, progressively increasing the scattering angle 2ϑ, the sequence of Bragg peaks in the q-range $(1.50–4.50\ \text{Å}^{-1})$ could be easily individuated. In this case, the pattern collected at the highest angle ($2\vartheta = 11.00°$) includes all the structural information contained in those acquired at lower angles.

The characteristic crystallization time is usually defined in two alternative ways, namely either as the time corresponding to half process (when 50% of the final amount of crystallites has been formed) or as the time corresponding to the maximum transformation speed (inflection point of the growth curve). However, when the crystallization follows a sigmoidal growth, these two quantities coincide and any ambiguity is removed. In this study, CCT is measured by fitting the experimental points by a sigmoidal curve from which the inflection point is calculated by imposing that, in correspondence of that instant, the second derivative of the curve equals zero.

RESULTS

To calculate the crystallites average size from a diffraction pattern, an equation based on the Laue relations (equivalent to the Scherrer formula that is valid for the angular dispersive X-ray diffraction mode only) was used[13]:

$$\frac{1}{2}tq_2 = (n+1)\pi \quad \text{and} \quad \frac{1}{2}tq_1 = (n-1)\pi \qquad (2)$$

where t is the crystallites average diameter; q_1 and q_2 are the interference function zeros adjacent to the function maximum ($q_1 < q_2$); n is the order of the interference function peaks (the parameter that labels the features of the "sinc" interference function). The grain size, $t = 4\pi/(q_2 - q_1)$, is obtained by combining these two equations and can be simplified assuming a triangular shape of the interference peak (the same approximation adopted by Scherrer), thus becoming: $t \cong 2\pi/\sigma_{[hkl]}$, where $\sigma_{[hkl]}$ is the standard deviation of the [hkl] peak intensity distribution due to the crystallite finite size. Once the contributions to the peaks broadening because of the limited instrumental resolution (that is, to both angular and energy spreads) are corrected, the relation between t and $\sigma_{[hkl]}$ can be used to calculate the former.

Ex situ EDXRD Measurements

Series of EDXRD measurements were performed *ex situ* on the cement precursor powders 1 and 2 and chitosan (38.2
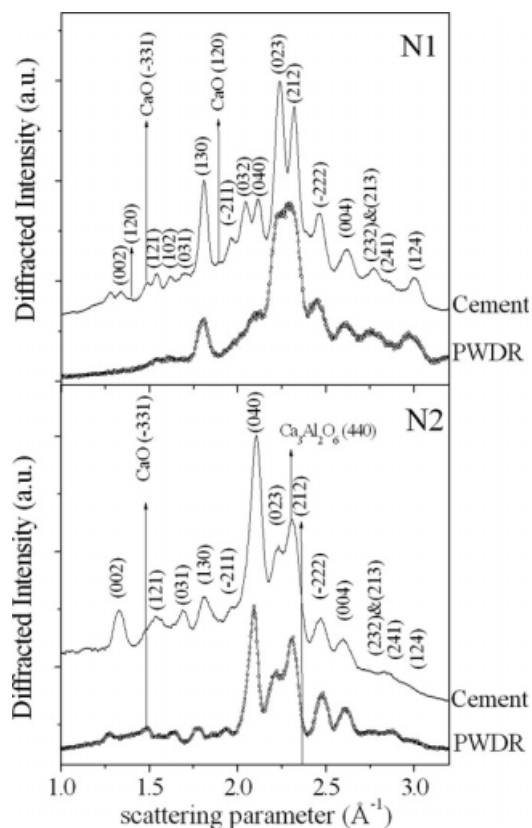

Figure 1. EDXRD patterns collected from the precursor powders 1 and 2 (continuous lines) and from the final cements 1 and 2 (line dots) under the same experimental conditions. The crystalline contributions are labeled.

and 478 kDA). The diffraction signal produced by pure chitosan is weak and appears as an X-ray amorphous diffuse halo. Both cement precursor powders are composed of the same main phase, $Ca_4(PO_4)_2O$ (Sys. Monoclinic, S.G.: $P2_1$ (4)[14]), and of CaO (Sys. Cubic, S.G.: $Fm\bar{3}m$ (225)[14]) phase. Moreover, the cement powder 2 also contains the $Ca_3Al_2O_6$ phase (Sys. Orthorombic, S.G.: not defined[14]).

Starting from the precursor powders 1 and 2, two different cements (cements 1 and 2) were produced *ex situ* and characterized by the EDXRD method. In Figure 1, the so-obtained diffraction spectra (line dots) are compared with the patterns of the precursor powders (continuous lines) under the same experimental conditions (scattering angle and collimation slits aperture). The $Ca_4(PO_4)_2O$ peaks are labeled in Figure 1, and furthermore, in this q region, the higher resolution and the long counting time allowed to detect signals produced by the crystalline CaO. For powder 2 and, consequently, for cement 2 (Figure 1, lower part), the $Ca_3Al_2O_6$ 100% relative intensity (440) peak was also detected.

As can be seen from Figure 1, the peak width for final products is much reduced, and the relative intensities of the Bragg reflections are varied, suggesting a primary crystallization process taking place on the pastes hardening. Moreover, the higher crystalline degree of the final products is
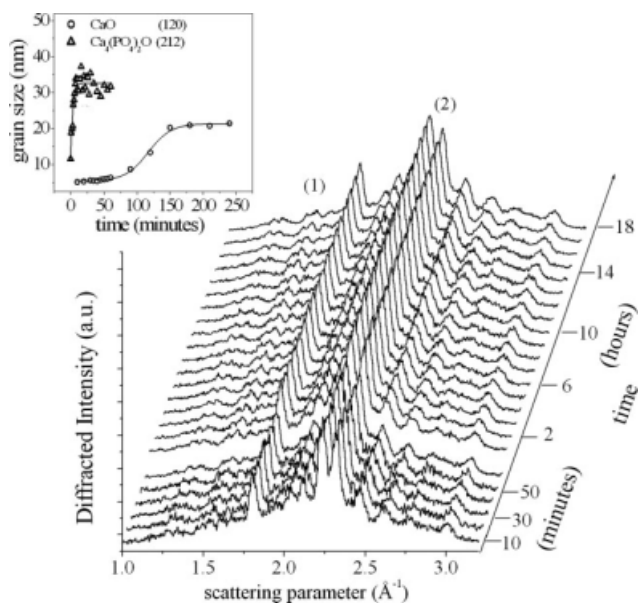
Figure 2. Sequences of EDXRD patterns, collected as a function of the scattering parameter and of time, during the hardening of cement 1. In the inset, the grain size time evolution for two phases, composing the precursor powder 1, is shown.

evidenced by the presence of more resolved Bragg reflections, particularly in cement 1.

After this preliminary characterization, *in situ* EDXRD studies were performed under the same experimental conditions.

In situ EDXRD Measurements

Precursor Powder 1. To perform *in situ* time-resolved diffraction measurements, the following experimental conditions were kept the same: energy of the X-ray beam, collimation slits apertures, and sample positioning. However, shorter acquisition times are required to accurately monitor the setting and hardening process *in situ*, and therefore, a lower scattering angle was chosen to perform the measurements. In fact, the data collection at $2\vartheta = 7.00°$ allowed to explore the $(1.00 \text{ Å}^{-1} < q < 3.50 \text{ Å}^{-1})$ q-range of interest, in which the difference between the precursor powders and final cements is remarkable, while maximizing the scattered intensity.

Then, cements 1 and 2 were prepared, and their diffraction patterns were collected every 60 s during the first 10 min, every 2 min for another 20 min, every 5 min until the first hour of setting, and every hour for the remaining hours. In this way, it was possible both to detect the crystallization process at the early stages of setting and to observe an eventual slower secondary crystallization. In Figure 2, the sequences of diffraction patterns for cement 1, collected as a function of the scattering parameter and of time (3D maps), are shown.

The patterns during the first hour of acquisition have been summed up (every 10 min) to increase the signal-to-noise ratio. However, to follow in real time the crystallization process associated to the cement's hardening, an accurate analysis of each EDXRD pattern was performed, calculating the time evolution of the peaks intensity and width. In particular, for cement 1, two peaks representative of the two different components constituting the precursor powder were chosen to follow the evolution. In the inset of Figure 2, the grain size time evolution of the two phases is plotted. The peak labeled as (1) corresponds to CaO (120), and peak (2) to the (212) $Ca_4(PO_4)_2O$. As visible, both crystallizations are characterized by a sigmoidal growth, but the characteristic times are much different. The CaO crystallization time is calculated to be $\tau_{(CaO)} = (116 \pm 30)$ min, whereas the $Ca_4(PO_4)_2O$ crystallization takes place in a much shorter characteristic time, $\tau_{(Ca4(PO4)2O)} = (1.9 \pm 1.0)$ min (Table I). Furthermore, no intensity variation of these peaks was observed, indicating that the process is a primary crystallization, that is, growth of initially crystalline material. Moreover, the characteristic grain dimensions were calculated. For the TetCP phase, the initial average grain dimension was $(12 \pm 1 \text{ nm})$, growing up to $(32 \pm 1 \text{ nm})$ during the crystallization process, whereas the CaO phase was formed by smaller domains, the initial average dimension being 5 nm and growing up to $(21 \pm 1 \text{ nm})$ (Table I).

Precursor Powder 2. The same analysis, described previously, was performed on the sequence of diffraction patterns collected on cement 2 hardening, plotted in Figure 3.

The accurate investigation of each EDXRD pattern in Figure 3 allowed to detect the formation of an intermediate phase, appearing 3 h after the beginning of the process, lasting 4 h, and then, disappearing. In the inset of Figure 3, the q-region containing a novel crystalline reflection (at $q = 2.18 \pm 0.01 \text{ Å}^{-1}$), evidenced by an arrow, which can be associated to such intermediate phase, is highlighted. The diffraction patterns are shifted in intensity for clarity. This peak corresponds to whitlockite–tricalcium phosphate (Sys.

TABLE I. Characteristic Crystallization Time and Grain Size Evolution on Hardening of Cements 1, With and Without Addition of Chitosan

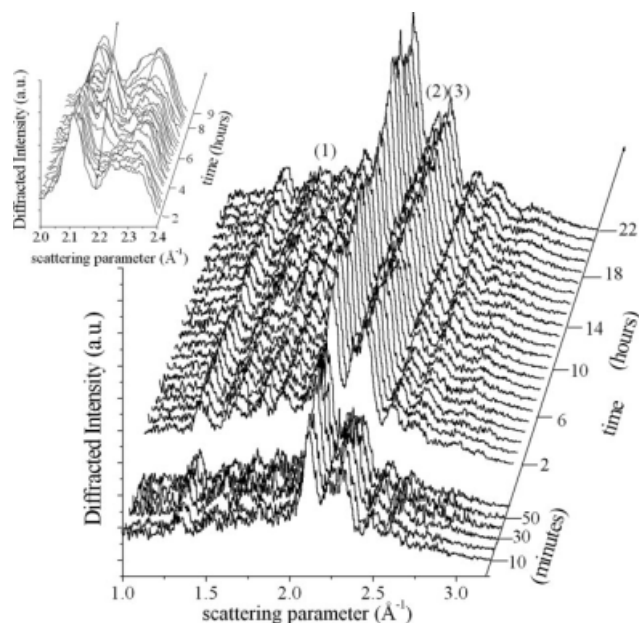| Cement 1	Characteristic Crystallization Time, τ (min)	Initial Average Grain Size (nm)	Final Average Grain Size (nm)
CaO	116 ± 30	5	21
$Ca_4(PO_4)_2O$	1.9 ± 1.0	12	32
Cement 1 with chitosan 38.2 kDa			
CaO	440 ± 30	5	24
$Ca_4(PO_4)_2O$	30 ± 5	13	33
Cement 1 with chitosan 478 kDa			
CaO	415 ± 30	6	11
$Ca_4(PO_4)_2O$	71 ± 5	21	27

Figure 3. Sequences of EDXRD patterns, collected as a function of the scattering parameter and of time, during the hardening of cement 2. In the inset, a specific q-space is highlighted to evidence the formation of a new phase, occurring on the hardening process.

Figure 4. Grain size time evolution of three phases, composing the precursor powder 2, during cement 2 hardening. The CaO crystallization curve could be divided in two characteristic periods: (a) inhibition of crystallization and (b) sigmoidal growth.

Rhombohedral, S.G.: R $\bar{3}$c[14]), 100% relative intensity (210) peak.

Furthermore, the CaO (120) (Figure 3, peak 1), the $Ca_4(PO_4)_2O$ (023) (Figure 3, peak 2), and the $Ca_3Al_2O_6$ (440) (Figure 3, peak 3) reflections were monitored in real time on the hardening of cement 2. TetCP and calcium aluminate crystallize with similar characteristic times ($\tau_{(Ca4(PO4)2O)}$ = (2.4 ± 1.0 min) and $\tau_{(Ca3Al2O6)}$ = (2.9 ± 1.0 min)) (Figure 4), and their crystallization can be well fitted by a sigmoidal growth, whereas the CaO (120) crystallization consists of two distinct processes [Figure 4(a,b)]: a first-order exponential decay (a) corresponds to the inhibition of the CaO phase crystallization, in which the crystalline grain size diminishes from (28 ± 1 nm) to (9 ± 1 nm). The characteristic time of this first process ($\tau_{(CaO\ (a))}$ = (11.3 ± 1.0 min)) perfectly coincides with the saturation times (11 min) for both the TetCP and the $Ca_3Al_2O_6$ grain growth. Afterward, when the main phases reached saturation, the crystallization of the latter component occurs. The second process is well fitted by a sigmoidal growth (b), the characteristic time of this evolution being $\tau_{(CaO(b))}$ = (85 ± 5 min), and the CaO grains grow from (9 ± 1 nm) up to (20 ± 1 nm) (Table II).

As can be seen from Figure 4, the average grain dimensions for TetCP increased from (12 ± 1 nm) up to (22 ± 1 nm), whereas for calcium aluminate from (20 ± 1 nm) up to (44 ± 1 nm) on cement 2 hardening.

Precursor Powder 1 with Addition of Chitosan. Cement samples were prepared inside the sample holder of the diffractometer by adding 0.01 g of low- or high-molec-
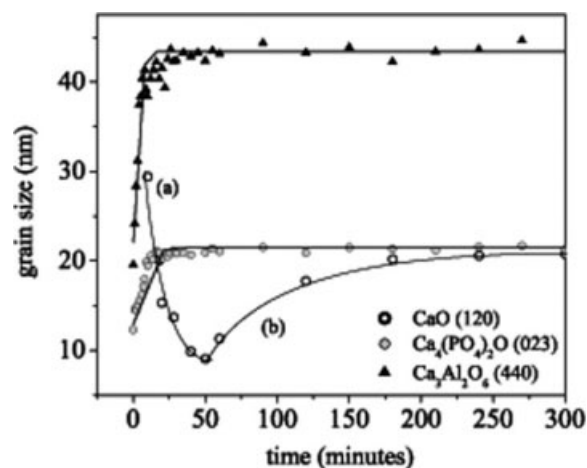
ular weight chitosan (38.2 and 478 kDA) to 0.4 g of the precursor powder 1 and then adding 0.2 mL of hardening liquid. The so-obtained samples were intensively mixed for about 1 min before the EDXRD acquisition. Subsequently, the occurring structural modifications were monitored in real time, collecting the sequences of diffraction patterns. The acquisition time of each pattern was set at 60 s for the first hour, and the overall observation time was 72 h. Comparing the so-obtained final products and the final cement 1, some differences can be observed. In Figure 5, the patterns collected under the same experimental conditions on cement 1 (A), final cement 1 with chitosan (38.2 kDa) addition (B), and final cement 1 with chitosan (478 kDa) addition (C) are plotted as a function of the scattering parameters. Spectra (A) and (B) are almost perfectly overlapping, all Bragg reflections being coincident, despite the relative intensities of the crystalline phases are not always comparable. However, this parameter could be influenced by the mixing procedure, inducing crystallization along a

TABLE II. Characteristic Crystallization Time and Grain Size Evolution on Hardening of Cements 2, With and Without Addition of Chitosan

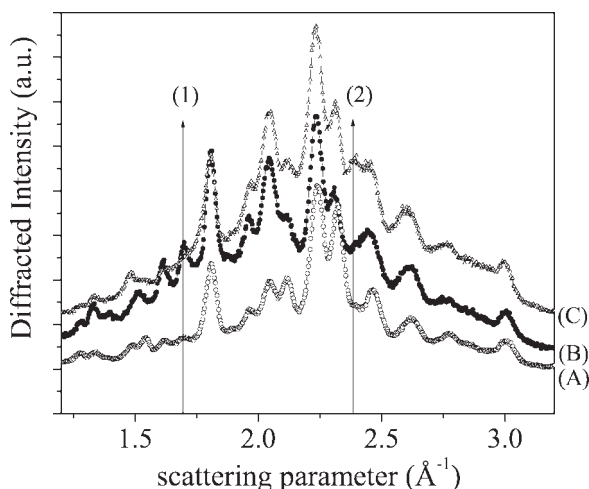| Cement 2	Characteristic Crystallization Time, τ (min)	Initial Average Grain Size (nm)	Final Average Grain Size (nm)
CaO	11.3 ± 1.0; 85 ± 5	28	20
$Ca_4(PO_4)_2O$	2.4 ± 1.0	12	22
$Ca_3Al_2O_6$	2.9 ± 1.0	20	44
Cement 2 with chitosan 38.2 kDa			
$Ca_4(PO_4)_2O$	28 ± 5	8	18
$Ca_3Al_2O_6$	24 ± 5	8	17
Cement 2 with chitosan 478 kDa			
$Ca_4(PO_4)_2O$	31 ± 5	8	15
$Ca_3Al_2O_6$	30 ± 5	8	10

Figure 5. EDXRD patterns collected as a function of the scattering parameter from cement 1 (A), cement 1 with the addition of chitosan 38.2 kDa (B), and cement 1 with the addition of chitosan 478 kDa (C).

certain crystalline direction and, therefore, affecting the final intensity proportions between the crystalline reflections. Alternatively, if the orientation is random, the diffracted intensity would be dominated by the crystallites having the largest size. In the former case, such crystallites would produce the most intense peaks and, therefore, would alter the intensity ratio between the peaks.

Furthermore, on pattern (C), along with the variation of the relative intensities, the disappearance of a pre-existent Bragg reflection (Figure 5, arrow 1, $q = (1.70 \pm 0.01$ Å^{-1})) and the appearance of a new peak (Figure 5, arrow 2, $q = (2.39 \pm 0.01$ Å^{-1})), attributable to (-110) $Ca_3(PO_4)_2$ (100% relative intensity, Sys. Rhombohedral, S.G.: R $\bar{3}$m[14]), can be observed.

In Figure 6, the grain size time evolution for $Ca_4(PO_4)_2O$ and CaO phases during the hardening of cement 1 with the addition of low- and high-molecular weight chitosan is plotted. Figure 6(A) corresponds to the addition of chitosan (38.2 kDa). As visible, both crystallizations are characterized by a sigmoidal growth, although the characteristic times are much different. A similar result was obtained for the hardening of cement 1 without chitosan. The CaO crystallization time is calculated to be $\tau_{(CaO)}$ = $(440 \pm 30$ min), whereas the $Ca_4(PO_4)_2O$ phase evolves with a much shorter characteristic time, $\tau_{(Ca4(PO4)2O)}$ = $(30 \pm 5$ min) (Table 1). Therefore, one can conclude that the addition of chitosan (38.2 kDa) to the mixture leads to a decrease in the rate of the crystallization process, and this effect is more evident for the TetCP phase. As to the grain growth, the average grain dimensions for CaO increased from $(5 \pm 1$ nm) up to $(24 \pm 1$ nm), whereas for the TetCP from $(13 \pm 1$ nm) up to $(33 \pm 1$ nm).

Subsequently, the hardening of cement 1 with the addition of chitosan (478 kDa) was studied [Figure 6(B), where the crystallization dynamics are reported]. Comparing the characteristic crystallization times with respect to the addi-

tion of chitosan (38.2 kDa), it can be noticed that the CaO (120) dynamics is preserved, $\tau_{(CaO)}$ = $(415 \pm 30$ min), despite the final grain size is now much reduced. Indeed, the initial grains are about $(6 \pm 1$ nm), comparable with the CaO grains, obtained when chitosan (38.2 kDa) is added, and they turn out to be about $(11 \pm 1$ nm) when chitosan (478 kDa) is added. Furthermore, the crystallization of $Ca_4(PO_4)_2O$ (212) is much slower than before, $\tau_{(Ca4(PO4)2O)}$ = $(71 \pm 5$ min), and also in this case, the grain size is affected by the addition of chitosan (478 kDa). Indeed, the initial grain dimension of $Ca_4(PO_4)_2O$ (212) is $(21 \pm 1$ nm), and it slightly grows up to $(27 \pm 1$ nm), when the crystallization process is concluded (Table I).

Precursor Powder 2 with Addition of Chitosan. As previously described for cement 1, different cement samples were prepared inside the sample holder of the diffractometer by adding 0.01 g chitosan (38.2 or 478 kDa) to the precursor powder 2. After that, to this mixture, the hardening liquid was added, and an intensive mixing for approximately 1 min was performed. Subsequently, the structural modifications that occur were monitored in real time, in the same way and under the same experimental conditions as before. Comparing the so-obtained final products and the final cement 2, some differences can be observed. In Figure 7, the patterns collected on final cement 2 (A), final cement 2 with chitosan (38.2 kDa) addition (B), and final cement 2 with chitosan (478 kDa) addition (C) are plotted as a function of the scattering parameters. Spectra (A) and (B) are almost perfectly overlapping, the relative intensities of the crystalline phases being comparable, whereas spectrum (C) presents some differences, evidenced in figure by the arrows. Indeed, the (031) $Ca_4(PO_4)_2O$ reflection is somewhat shifted toward higher q values (peak (1) at $q = (1.72 \pm 0.01$ Å^{-1})), which might be due to a reticular compressive stress. Moreover, the presence of a peak (2) at $q = (2.05 \pm 0.01$ Å^{-1}) can be attributed to the (032) $Ca_4(PO_4)_2O$. These experimental observations lead to a conclusion that the addition of high-molecular weight chitosan affects the crystallization along the [03l] directions.

In Figure 8, the grain size time evolution of the $Ca_4(PO_4)_2O$ and $Ca_3Al_2O_6$ phases during the hardening of

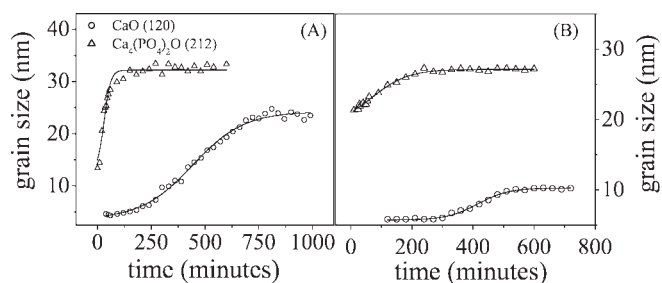**Figure 6.** Grain size time evolution for $Ca_4(PO_4)_2O$ and CaO phases during the hardening of cement 1 with: (A) addition of chitosan 38.2 kDa, (B) addition of chitosan 478 kDa.
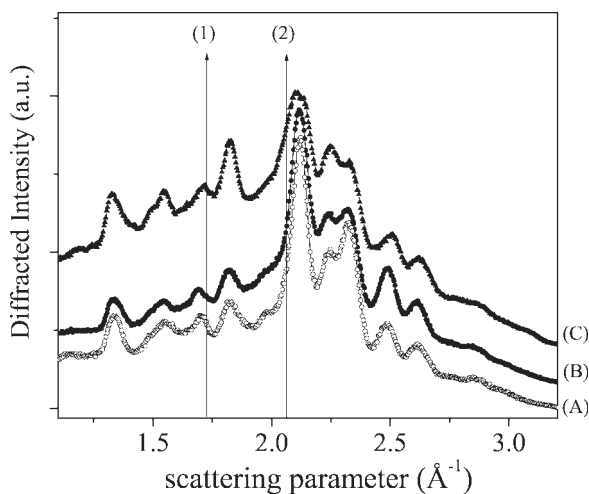
Figure 7. EDXRD patterns collected as a function of the scattering parameter from cement 2 (A), cement 2 with addition of chitosan 38.2 kDa (B) and cement 2 with addition of chitosan 478 kDa (C).

cement 2 with the addition of low- (A) and high-molecular weight chitosan (B), respectively, is plotted.

In this case, it was not possible to estimate the time evolution of CaO (120), the peak being scarcely resolved, and hence, the distribution of its full width half maximum values appearing random. However, $Ca_4(PO_4)_2O$ (040) and $Ca_3Al_2O_6$ (440) were monitored, and their crystallization is characterized by a sigmoidal evolution. The addition of chitosan (38.2 kDa) led to a decrease in the rate of the hardening process, the characteristic times being $\tau_{(Ca4(PO4)2O)}$ = (28 ± 5 min) and $\tau_{(Ca3Al2O6)}$ = (24 ± 5 min) (Table 2). The time evolution of the two phases coincides well with that previously observed in the case of hardening of cement 2 without chitosan. The $Ca_4(PO_4)_2O$ grains grow from 8 nm up to 18 nm; and the $Ca_3Al_2O_6$ grains grow from 8 nm up to 16.5 nm.

Subsequently, the hardening of cement 2 with the addition of chitosan (478 kDa) was studied [Figure 8(B)]. Also in this case, the CaO reflection was weak to be accurately fitted, and only the $Ca_4(PO_4)_2O$ (040) and the $Ca_3Al_2O_6$ (440) reflections were evaluated. The time evolution of the primary crystallization, shown in Figure 8(B), is well fitted
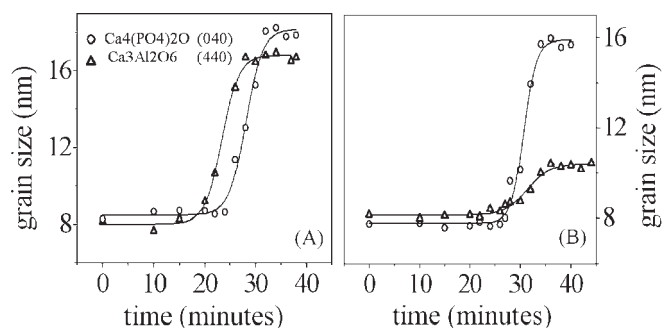

Figure 8. Grain size time evolution for $Ca_4(PO_4)_2O$ and $Ca_3Al_2O_6$ phases during the hardening of cement 2 with: (A) addition of chitosan 38.2 kDa, (B) addition of chitosan 478 kDa.

by a sigmoidal growth for both phases, and as previously observed, the characteristic times are comparable, $\tau_{(Ca4(PO4)2O)}$ = (31 ± 5 min) and $\tau_{(Ca_3A_{12}O_6)}$ = (30 ± 5 min) (Table 2). However, the addition of chitosan (478 kDa) strongly influences the grain dimensions, particularly those of the calcium aluminate. In fact, the initial average dimensions of both phases are comparable to those previously observed, but the final crystallite size is smaller, that is, for $Ca_4(PO_4)_2O$ and $Ca_3Al_2O_6$ being (15 ± 1 nm) and (10 ± 1 nm), respectively.

Moreover, highlighting the q-region 1.20/1.50 Å^{-1}, it was possible to detect the formation of an intermediate, identified as hydroxyapatite (HA) phase (hexagonal system, S.G.:P6$_3$/m^{14}). In particular, the onset of the (110) Bragg reflection at q = (1.35 ± 0.01) Å^{-1} is visible when cement 2 is mixed with chitosan (38.2 kDa) (Figure 9, left side) and chitosan (478 kDa) (Figure 9, right side). It is worth noticing that, in the former case, the HA crystallization is clearly visible after 20 min from the beginning of the process, and the same reflection is no longer visible already after 30 min, that is, it lasts only 10 min. Conversely, when chitosan (478 kDa) is added, the rate of the HA formation is much slower: the (110) reflection appears 30 min after the beginning of the process and lasts about 1 h.

pH and Compressive Strength Measurements

Because both cements contain basic TetCP and CaO compounds, it is important to follow their pH time evolution during the process of hardening. These results are shown in Figure 10. As can be seen, for cement 1, pH is around 6.5 at the beginning of hardening, then reaching 7.2, whereas for cement 2, pH value does not change significantly, being around 6.5 at the beginning and 6.7 after 22 days. Therefore, pH of both cements is very close to neutral.
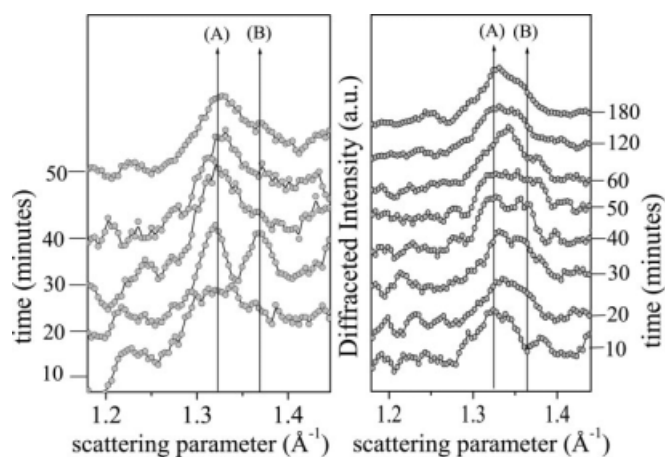

Figure 9. Highlights of EDXRD patterns collected as a function of time during the hardening of cement 2 with chitosan 38.2 kDa (left side) and with chitosan 478 kDa (right side). The arrows point out the presence of the (A) $Ca_4(PO_4)_2O$ (002) reflection and the formation and disappearance of the (B) $Ca_{10}(Ca_4)_6(OH)_2$ (110) contribution.

Figure 10. pH time evolution for cements 1 and 2.
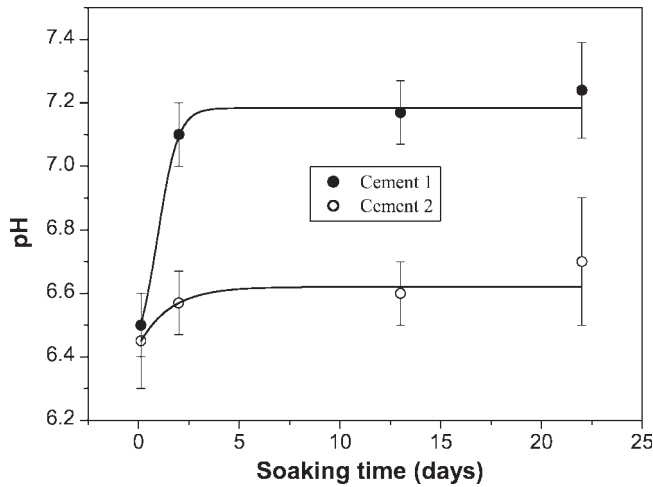

Figure 12. SEM micrograph of cement 1. Magnification 2,55 K×.

In Figure 11, the time evolution of another important characteristic of cements, the compressive strength, is shown. As can be observed, the compressive strength of cement 1 reached 68 MPa after 22 days of hardening, whereas the compressive strength of cement 2 is much higher, reaching 102 MPa after the same time period.

SEM Measurements

In Figures 12–14, the SEM micrographs of cements 1 and 2 are shown. As can be seen, cement 1 has more homogeneous structure (Figure 12), characterized by micro- and nanopores, whereas the surface morphology of cement 2 is slightly different: because it is visible at high magnification (Figure 13), it is composed of lamellar-like crystals with submicro- and nanopores. The same cement 2, but in the presence of chitosan, has another morphology—it is composed of smoothed grains, covered by chitosan film. Separate chitosan particles can also be distinguished. The porosity is lower compared with that of the same cement
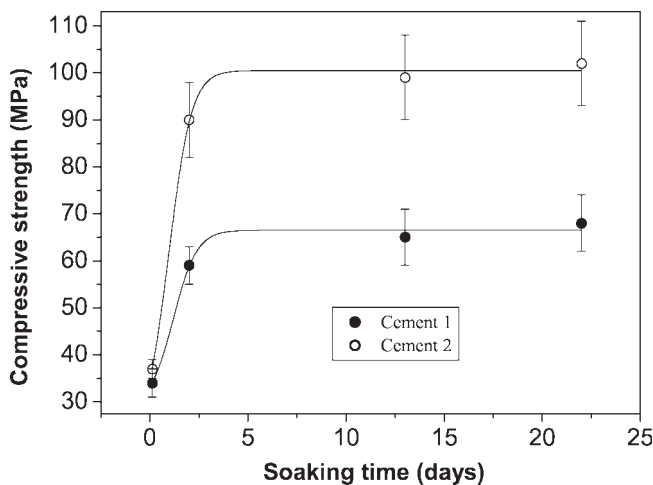
without chitosan addition. Chitosan seems to have an aggregating and smoothing effect. In Figure 14, cement and chitosan particles conglomerated all together can be observed.

DISCUSSION

Despite the numerous literature data available in the field of calcium phosphate bone cements, the mechanism and kinetics of their hardening, in most cases, is unknown. We applied the EDXRD technique to follow the phase transformations and kinetics during hardening of two new formulations we propose.

In the case of cement 1, no intermediate phases were detected, likely because the process is too fast to be revealed by the EDXRD technique. Not even the addition of chitosan (38.2 kDa), which retards the hardening process, allowed to register any intermediate phase, being the crystallization only slightly slower. Conversely, the
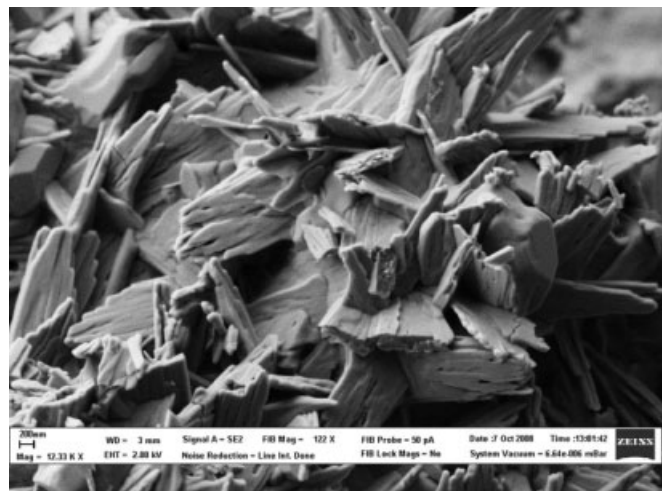

Figure 11. Compressive strength time evolution for cements 1 and 2.

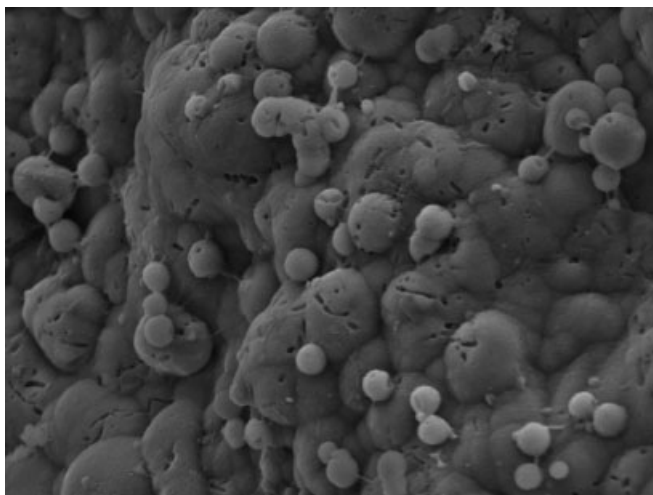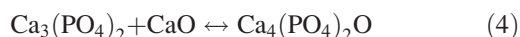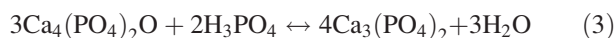**Figure 13.** SEM micrograph of cement 2. Magnification 12,33 K×.

Figure 14. SEM micrograph of cement 2 with high-molecular weight chitosan addition. Magnification 6,16 K×.
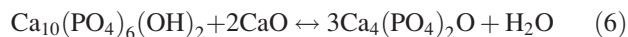
addition of chitosan (478 kDa) slows down the hardening process, so that tricalcium phosphate intermediate phase can be observed (Figure 5). It is likely that, in this case, the following reactions take place:

$$3Ca_4(PO_4)_2O + 2H_3PO_4 \leftrightarrow 4Ca_3(PO_4)_2 + 3H_2O \quad (3)$$

$$Ca_3(PO_4)_2 + CaO \leftrightarrow Ca_4(PO_4)_2O \quad (4)$$

At first, TetCP (main component of both cement powders) dissolves in the acidic hardening liquid. Simultaneously with TetCP, CaO also dissolves. The $Ca_3(PO_4)_2$ compound, formed according to reaction (3), interacts with CaO (taken in 10% excess), resulting in the final TetCP phase formation [reaction (4)].

In the case of cement 2, the formation of an intermediate (again tricalcium phosphate) was observed even without the addition of chitosan (Figure 3). Evidently, the decrease in the rate of the process, which allowed the detection of the intermediate phase, was due to the presence of the $Ca_3Al_2O_6$ admixture in the precursor cement powder.

Then, when chitosans (38.2 and 478 kDa) are added to cement 2, the formation of another intermediate phase, HA, is evidenced (Figure 9). The following reactions, likely taking place during the hardening, can be proposed:

$$5Ca_4(PO_4)_2O + 2H_3PO_4 \leftrightarrow 2Ca_{10}(PO_4)_6(OH_2) + H_2O \quad (5)$$

$$Ca_{10}(PO_4)_6(OH)_2 + 2CaO \leftrightarrow 3Ca_4(PO_4)_2O + H_2O \quad (6)$$

As can be seen from Figure 9, in the case of the low-molecular weight chitosan, the entire process of appearance and disappearance of crystalline HA lasts about 10 min, whereas in the case of the high-molecular weight chitosan, the same process lasts about 1 h, indicating that chitosan (478 kDa) slows down the process more than chitosan (38.2 kDa).

It should be mentioned that HA and tricalcium phosphate phases have similar properties and are easily converted one into another under suitable conditions.

The fact that the presence of calcium aluminate contributes to the decrease in the rate of the process is confirmed also by the following results: from Figure 2 (cement 1), one can see that already 8 min after the beginning of the hardening process, the crystallization of the TetCP particles is completed, whereas the CaO particle growth starts. The CaO crystallization finishes after about 150 min of the hardening process. The increase in the crystallized CaO amount likely leads to some increase in the pH value of the cement, from 6.5 to 7.1 (Figure 11). Unlikely, for cement 2 (Figure 4), the particle growth of TetCP and calcium aluminate takes place simultaneously with the decrease in the CaO particle size, that is, its dissolution. The TetCP crystallization process is concluded after about 25 min and only 50 min later the CaO crystallization starts. Furthermore, in this case, the CaO excess is minimal, which is confirmed by the slight increase in pH value for cement 2, from 6.5 to 6.6 (Figure 10).

In our previous investigation,[8] it was found that low-molecular weight chitosan inhibits the hardening process in the TetCP cements. In this study, we investigated the influence of both low- and high-molecular weight chitosan. The results obtained are summarized in Tables 1 and 2. In the case of cement 1, two characteristic crystallization times were deduced for CaO and TetCP, 116 and 2 min, respectively. The addition of chitosan (38.2 kDa) leads to a four times decrease in the CaO crystallization rate and to a 15 times decrease in the TetCP crystallization rate. When chitosan (478 kDa) is added, the same result is obtained for CaO, whereas for TetCP, the crystallization rate is decreased by 35 times.

In the case of cement 2, two characteristic crystallization times were deduced for TetCP and $Ca_3Al_2O_6$, both within 3 min. The addition of chitosan (38.2 kDa) leads to a 10 times decrease in the crystallization rate of both phases, and the same result is obtained when chitosan (478 kDa) is added.

One of the defects of CPCs is that they are usually brittle, possessing poor mechanical properties. To improve this characteristic, continuous efforts have been made.[15,16] A new high-strength cement, reported in Ref. 15, was prepared from calcium phosphate and calcium aluminate for potential use in bone and joint repair applications. This cements attained the compressive strength of about 100 MPa after 4 weeks of hardening. The authors[15] explain the changes in strength over time by the continued hydration of calcium aluminate and its conversion into hydrated calcium aluminate phases, $Ca_3Al_2O_6 \times XH_2O$.

CPCs represent a good correction technique for the non–load-bearing bone fractures and defects and seem to be very promising materials for bone grafting applications.[17] In the latter case, a mechanical requirement may be stated that the strength of the set cements must be at least as high as that of bones. However, in practice, the strength of the cements is lower than that of bones, teeth, or sintered calcium phosphate ceramics and should, therefore, be improved. For example, elevated compressive strength

would be applicable in cranioplasty for the regions requiring significant soft-tissue support and could be important in orthopedic and dental applications.[17]

In this work, the compressive strength of cement 2 (with calcium aluminate addition) reaches about 100 MPa after 3 weeks of hardening, and it is also likely connected to the formation of hydrated calcium aluminate phases. However, it should be noticed that the X-ray diffraction method applied in this work cannot evidence clathrate water complexes and therefore cannot indicate their formation.[18]

It should be underlined that classical calcium phosphate-based cements reported in the literature are mainly nonresorbable, that is, HA is formed as the final phase.[7,8,15] In this work, instead, resorbable $Ca_4(PO_4)_2O$ is registered as the final phase. This result is achieved because of the presence of the CaO excess (leading to its presence also in the final product), which contributes to the shift of the reaction products from HA to the TetCP formation.

CONCLUSIONS

Two new cement formulations, based on TetCP, are obtained, both having pH close to 7. Cement 1 has a compressive strength of about 70 MPa, whereas the compressive strength of cement 2 is much higher, about 100 MPa. The latter result is attained thanks to the $Ca_3Al_2O_6$ addition to the initial cement powder. High-strength cement 2 could be an alternative to the low-strength bioresorbable brushite cements (10–12 MPa).[19]

The formation of the TetCP final phase during the cement's hardening could be described by the real-time observation of the structural changes allowed by EDXRD. It takes place because of the presence of the CaO excess in the precursor powder. The mechanism of hardening includes the stages of the reaction between TetCP and the hardening liquid, resulting in the formation of an intermediate phase, followed by its fast interaction with CaO, leading to the final formation of the TetCP-based cement. Intermediate phases can be either tricalcium phosphate or HA, depending on the presence of chitosan or other admixtures in the precursor powder.

Both low- and high-molecular weight chitosan inhibit the cements hardening. Chitosan (478 kDa) slows down the hardening more than chitosan (38.2 kDa).

REFERENCES

1. LeGeros RZ, Chohayeb A, Shulman A. Apatitic calcium phosphates: Possible dental restorative materials. J Dent Res 1982;62:343.
2. Brown E, Chow LC. A new calcium phosphate setting cement. J Dent Res 1983;62:672.
3. Bohner M, Gbureck U, Barralet JE. Technological issues for the development of more efficient calcium phosphate bone cements: A critical assessment. Biomaterials 2005;26:6423–6429.
4. Bohner M. Physical and chemical aspects of calcium phosphates used in spinal surgery. Eur Spine J 2001;10:114–121.
5. Kenny SM, Burggy M. Bone cements and fillers: A review. J Mater Sci Mater Med 2003;14:923–938.
6. Liu C, Shen W, Gu Y, Hu L. Mechanism of the hardening process for a hydroxyapatite cement. J Biomed Mater Res 1997;35:75–80.
7. Generosi A, Smirnov VV, Rau JV, Rossi Albertini V, Ferro D, Barinov SM. Phase development in the hardening process of two calcium phosphate bone cements: An energy dispersive X-ray diffraction study. Mater Res Bull 2008;43:561–571.
8. Rau JV, Generosi A, Smirnov VV, Ferro D, Rossi Albertini V, Barinov SM. Energy dispersive X-ray diffraction study of phase development during hardening of calcium phosphate bone cements with addition of chitosan. Acta Biomaterialia 2008;4:1089–1094.
9. Carey LE, Xu HH, Simon CG Jr, Takagi S, Chow LC. Pre-mixed rapid-setting calcium phosphate composites for bone repair. Biomaterials 2005;26:5002–5014.
10. Barinov SM, Shevchenko VY. Strength of Engineering Ceramics. Moscow: Science; 1996.
11. Felici R, Cilloco F, Caminiti R, Sadun C, Rossi V. Italian Patent No. RM 93 A 000410; 1993.
12. Caminiti R, Rossi Albertini V. The kinetics of phase transition observed by energy dispersive x-ray diffraction. Int Rev Phys Chem 1999;18:263–299.
13. Patterson AL. The Scherrer formula for X-ray particle size determination. Phys Rev 1939;56:978–982.
14. International Centre for Diffraction Data, Database JCPDS (2000).
15. Roemhildt ML, McGee TD, Wagner SD. Novel calcium phosphate composite bone cement: Strength and bonding properties. J Mater Sci: Mater Med 2003;14:137–141.
16. Yamamoto H, Niwa S, Hori M, Hattori T, Sawai K, Aoki S, Hirano M, Takeuchi H. Mechanical strength of calcium phosphate cement in vivo and in vitro. Biomaterials 1998;19: 1587–1591.
17. Dorozhkin SV. Calcium orthophosphate cements and concretes. Materials 2009;2:221–291.
18. Als-Nielsen J, McMorrow D. Elements of Modern X-ray Physics. New York: John Wiley and Sons; 2001.
19. Barralet JE, Grover LM, Gbureck U. Ionic modification of calcium phosphate cement viscosity. Part II: Hypodermic injection and strength improvement of brushite cement. Biomaterials 2004;25:2197–2203.